

Spectral reflectance variations of aubrites, metal-rich meteorites, and sulfides: Implications for exploration of (16) Psyche and other “spectrally featureless” asteroids

Steven D. DIBB¹ ^{*}, James F. BELL III¹, and Laurence A. J. GARVIE^{1,2}

¹School of Earth and Space Exploration, Arizona State University, Tempe, Arizona 85287, USA

²Buseck Center for Meteorite Studies, Arizona State University, Tempe, Arizona 85287, USA

*Corresponding author. E-mail: sd.dibb@gmail.com

(Received 06 July 2021; revision accepted 02 June 2022)

Abstract—The 350–2500 nm reflectance spectra of five enstatite achondrites (aubrites), five metal-rich chondrites (CBa, CBb, CH/CBb, and ungrouped), and seven sulfide mineral samples (three troilites, pyrrhotite, pentlandite, a mixture of pentlandite and chalcopyrite, and oldhamite) have been measured to search for spectral parameters that may offer insight into the surface composition of so-called “spectrally featureless” asteroids. Spectral data were acquired from powders, slabs, and hand samples. Aubrites exhibit high reflectance, generally positive slopes at visible wavelengths, and low-to-negative infrared slopes, consistent with E-/Xe-type asteroids. The metal-rich chondrites exhibit low reflectance, moderate visible slopes, and low near-infrared slopes, somewhat consistent with M-/X-complex asteroids. The metal-rich chondrites exhibit absorption features at ~900 nm arising from Fe²⁺-bearing silicates. Sulfides exhibit low to moderate reflectance and high visible and near-infrared slope, intermediate to the T- and L-type asteroids. The D-type asteroids, which have high visible and near-infrared slopes, are not well-matched by sulfides. Spectral data of the largest M-/X-type asteroid, (16) Psyche, are consistent with both powder from the Isheyevo CH/CBb chondrite and powder of meteoritic troilite. The data presented here will support interpretation of data returned from future spacecraft missions to “spectrally featureless” asteroids, like the Psyche, Lucy, and DART/Hera missions.

INTRODUCTION

Many asteroids exhibit relatively featureless reflectance spectra at visible to near-infrared wavelengths and have been variously categorized in different taxonomies in the past several decades (e.g., Bus & Binzel, 2002; Clark, Bus, Rivkin, McConnochie, et al., 2004; Clark, Bus, Rivkin, Shepard, et al., 2004; DeMeo et al., 2009; Tholen, 1984). In Tholen's taxonomy, the featureless, red-sloped (increasing reflectance with increasing wavelength) X-types were further separated into the E-, M-, and P-type asteroids on the basis of their visible wavelength albedos: E-types have visible albedos >0.3, M-types have visible albedos between 0.1 and 0.3, and P-types <0.1 (Tholen, 1984). These asteroids represent ~26% of the objects studied in the Eight-Color Asteroid Survey from which Tholen

created the taxonomy (Tholen, 1984; Zellner et al., 1985). In the Small Main-Belt Asteroid Spectroscopic Survey (SMASS), ~15% of asteroids studied were categorized into the “X-complex” and separated by principal component analysis of their 435–900 nm reflectance spectra into the Xe-, Xc-, Xk-, and X-types (Bus & Binzel, 2002). DeMeo et al. (2009) further developed the Bus taxonomy using spectral measurements out to ~2500 nm. While not fitting into the Bus-DeMeo X-complex, the T-, L-, and D- type asteroids are also relatively spectrally featureless and generally have steeper spectral slopes than the X-complex asteroids (DeMeo et al., 2009). We adopt the term “featureless” from Clark, Bus, Rivkin, Shepard, et al. (2004) to refer to any asteroid with a visible to near-infrared reflectance spectrum that is red-sloped and exhibits either no significant absorption features or subtle, weak features,

that is, $<5\%$ band depth. This includes the Tholen E-, M-, and P-types and the Bus-DeMeo X-, Xc-, Xe-, and Xk-type asteroids. We also include the Bus-DeMeo T-, L-, and D-types.

Visible to near-infrared spectra are among the few kinds of overlapping datasets between large numbers of asteroids and meteorites and therefore many authors have sought to establish connections between these two sets of objects using these datasets (e.g., Binzel & Xu, 1993; Cloutis et al., 1990; Gaffey & Kelley, 2004; Sunshine et al., 2008). However, because of their relatively featureless spectra, mineralogical interpretation of the surfaces of “featureless” asteroids is often inconclusive. Here, we present new visible to near-infrared reflectance spectra of materials that may be analogs for the surfaces of these asteroids. Our sample set contains five aubrites, seven sulfide minerals, and five metal-rich chondrites. These materials exhibit relatively featureless, red-sloped reflectance spectra and as such are plausible analogs for the surfaces of “spectrally featureless” asteroids due to physical and mineralogical properties (e.g., relatively high density, low FeO silicates). In addition to supporting telescopic observations of asteroids from Earth, robust libraries of visible to near-infrared spectra are critical for interpretation of data returned from future missions to “spectrally featureless” asteroids, such as the Psyche, Lucy, and Hera missions, which will carry visible to near-infrared imaging systems (Bell et al., 2016; Ferrari et al., 2021; Levison et al., 2016). The nature of any regolith on these asteroids is poorly constrained and so we report reflectance spectra of some of these materials in different physical forms (e.g., hand samples, slabs, different grain sizes) and over a range of phase angles to supplement future investigations of “featureless” asteroids. To support mineralogical interpretations of the spectra of these samples, we also present powder X-ray diffraction (XRD) data where possible. The combination of these two datasets will support interpretation of data from future space missions to members of these enigmatic asteroid taxa.

Tholen X-Type Asteroids

Many of the Tholen X-type asteroids are also categorized in the Bus-DeMeo taxonomy as X-complex asteroids. The Tholen E-types are roughly equivalent to the Bus-DeMeo Xe-types, while the Tholen M-types were categorized under each of the Bus-DeMeo X-complex subtypes (X-, Xe-, Xk-, and Xc-types). The Tholen P-types fall mostly within the Bus-DeMeo X- and Xk-types (DeMeo et al., 2009). Here, we discuss mineralogical interpretations of each of these asteroid types from the perspective of the Tholen E-, M-, and P-types.

The E-types have been linked to the enstatite achondrite meteorites (also known as aubrites) because of similar visible albedo and reflectance properties at near-infrared wavelengths (Clark, Bus, Rivkin, McConnochie, et al., 2004; Zellner et al., 1977). These meteorites required a significant degree of igneous processing, and therefore exploration of E-type asteroids could offer unique constraints on models of planetary formation (Watters & Prinz, 1979). E-type asteroids have been further distinguished into EI, EII, and EIII subtypes (Fornasier et al., 2008; Gaffey & Kelley, 2004). The EI asteroids are characterized by featureless, red-sloped spectra consistent with nearly Fe-free enstatite as seen in aubrites (Clark, Bus, Rivkin, McConnochie, et al., 2004). In contrast, the EII and EIII asteroids exhibit red-sloped spectra with some absorption features diagnostic of certain minerals. Absorptions at ~ 500 nm and ~ 960 nm in the spectra of EII asteroids are interpreted as originating from the calcium sulfide mineral oldhamite, which, if present, indicates a highly reducing formation environment (Clark, Bus, Rivkin, McConnochie, et al., 2004; Fornasier et al., 2008; Gaffey & Kelley, 2004; Watters & Prinz, 1979). Spectra of the EIII asteroids exhibit absorption features at ~ 900 nm consistent with Fe-bearing pyroxene, which would indicate a more oxidizing environment than that suggested by the EIIs. This discrepancy indicates that our understanding of the linkage between E-types and aubrites is incomplete (Clark, Bus, Rivkin, McConnochie, et al., 2004).

M-type asteroids are thought to have a significant metal component based on observations of density, emissivity, radar reflectivity, and spectral reflectance (e.g., Carry, 2012; Clark, Bus, Rivkin, Shepard, et al., 2004; Cloutis et al., 1990; Elkins-Tanton et al., 2020; Hardersen et al., 2011; Shepard et al., 2015). Density estimates for the M-types are typically greater than 3.2 g cm^{-3} , while radar albedos of many members of this class exceed 0.3, a threshold consistent with a surface dominated by metal (Carry, 2012; Shepard et al., 2015). The inferred presence of a large fraction of metal in most M-type asteroids indicates that they likely formed in a reduced environment and could be remnant core material from disrupted differentiated planetesimals or are perhaps stripped cores themselves.

Spectra of asteroid (16) Psyche exhibit subtle absorption features at ~ 900 nm consistent with low-Fe pyroxenes, which would be further consistent with a reduced formation environment (Fornasier et al., 2010; Hardersen et al., 2011). However, recent spectral observations of (16) Psyche by Sanchez et al. (2017) are consistent with much more Fe-rich pyroxene, suggesting that our understanding of the formation and nature of M-types is incomplete. Furthermore, some M-type

asteroids exhibit a weak absorption feature at 3 μm consistent with the presence of hydrated silicates, and thus are inconsistent with the interpretation that M-types are primarily metal, which might be expected for a remnant core (Rivkin et al., 1995, 2000).

The P-type asteroids are enigmatic as meteoritic analogs have so far not been recognized: they have been interpreted as possibly containing carbonaceous chondritic material, anhydrous silicates, phyllosilicates, ice, and/or unidentified opaque materials (Clark, Bus, Rivkin, Shepard, et al., 2004; Hiroi et al., 2004; Rivkin et al., 2002). These components are primarily inferred from the relatively low bulk density of these asteroids ($\sim 0.8\text{--}1.5\text{ g cm}^{-3}$), their orbital locations, and the near-total lack of absorption features in their visible to near-infrared spectra (Carry, 2012; Hanuš et al., 2017; Hiroi et al., 2004; Vernazza et al., 2015). A review of 22 P-type asteroid spectra by Fornasier et al. (2014) found that only one exhibited absorption features at visible wavelengths consistent with hydrated silicates, and observations of these asteroids at 3 μm have had mixed results, with most studies not observing any 3- μm absorptions for P-type asteroids (Emery & Brown, 2003; Jones et al., 1990; Lebofsky et al., 1990; Takir & Emery, 2012). One hypothesis for P-types (and the related D-type asteroids) is that they may be the sources for a significant amount of the interplanetary dust particles (IDPs) in terrestrial collections (Bradley, 2003; Vernazza et al., 2015). Roughly half of IDPs are classified as “chondritic porous” (CP) IDPs, which are composed predominately of Fe-poor pyroxene and olivine, sulfides, FeNi metal, glasses, and carbonaceous material (Bradley, 2003). The morphology of the component grains and the presence of solar flare tracks in IDPs suggests that these particles were formed during vapor-phase condensation of the solar nebula; some inclusions are likely presolar and could have formed in the atmospheres of other stars. Using microspectrophotometry, Bradley et al. (1996) established a connection between CP IDPs and the P- and D-type asteroids. If true, these asteroids would represent an unparalleled source for unprocessed, presolar material. P-type asteroids remain a subject of important study because of the uncertainty surrounding their origin and nature.

Bus-DeMeo D-, T-, and L-Type Asteroids and the Jupiter Trojans

The T-type asteroids are characterized by featureless, concave down spectra with moderate slope (DeMeo et al., 2009). Similar to T-types, L-type asteroids are characterized by reflectance spectra with steep visible slopes that shallow in the near-infrared,

producing an overall concave spectrum (DeMeo et al., 2009). Some L-types exhibit a subtle absorption feature in the near-infrared at $\sim 900\text{ nm}$ while others may exhibit a feature at 2 μm (DeMeo et al., 2009). Spectra of D-type asteroids are characterized by a very steep red slope, with some exhibiting a change to lower slope at near-infrared wavelengths (DeMeo et al., 2009).

The surface compositions of these three types of asteroids are poorly constrained. Britt et al. (1992) compared the T-types to laboratory reflectance spectra of troilite, while others have compared spectra of T- and D-type asteroids to the ungrouped carbonaceous chondrite Tagish Lake (e.g., Hiroi et al., 2001; Izawa et al., 2010). Finally, observations of L-type asteroids suggest a surface rich in spinel (as seen in calcium–aluminum inclusions), albeit at abundances greater than known meteorites (Burbine et al., 1992; Devogèle et al., 2018; Sunshine et al., 2008).

Analysis of the visible to near-infrared spectra of the Jupiter Trojan asteroids suggests that they are split into two spectral groups: a “red” group with spectra consistent with D-type asteroids, and a “less-red” group consistent with P-types (Emery & Brown, 2003; Emery et al., 2011, 2015). Due to a lack of any significant absorption features, mineralogical interpretations of the surface of these asteroids remains elusive. The densities of these asteroids are consistent with ice and organics, but the lack of definitive absorption features limits the abundance and nature of these possible components. Furthermore, whether the two Trojan spectral populations share a common origin is still under debate (e.g., Brown, 2016; Emery et al., 2015).

Spacecraft Exploration of “Featureless” Asteroids

One method to resolve the outstanding questions surrounding “featureless” asteroids is to send spacecraft to explore them. To date, only two “featureless” asteroids have been visited by a spacecraft: the European Space Agency’s Rosetta spacecraft encountered the E-/Xe-type asteroid (2867) Šteins and the M-/Xk-type asteroid (21) Lutetia in 2008 and 2010, respectively (Coradini et al., 2011; Keller et al., 2010). While (253) Mathilde has a relatively featureless spectrum consistent with C-type asteroids, its blue slope (decreasing reflectance with increasing wavelength) at visible to near-infrared wavelengths observed by the NEAR spacecraft (e.g., Clark et al., 1999) precludes it from the definition of red-sloped, “spectrally featureless” asteroids used in this study.

Fly-by observations of (2867) Šteins indicated the surface was largely enstatite-rich with a significant component of sulfide minerals (e.g., oldhamite—CaS) based on observations of a strong absorption feature

centered at ~ 490 nm. Asteroid (21) Lutetia's high density (~ 3.4 g cm $^{-3}$) and featureless, red-sloped spectrum indicate that it has a high metal abundance. The surface colors of both asteroids were observed to be spectrally homogeneous, which was interpreted as a lack of space weathering-induced spectral contrasts (Coradini et al., 2011; Keller et al., 2010).

The “featureless” asteroids are targets of multiple future space missions because of their potential as snapshots into the processes of solar system formation and planetary differentiation. These include the Psyche mission to the M-type asteroid, (16) Psyche; the Lucy mission, which will visit six large Jupiter Trojan asteroids, including P- and D-types; and the DART and Hera missions to the Xk-type near-Earth asteroid (65803) Didymos and its small moon. The Psyche and Lucy spacecraft will be equipped with multispectral imagers, while the Milani cubesat of the Hera mission will be equipped with a hyperspectral imager (Bell et al., 2016; Ferrari et al., 2021; Levison et al., 2016). Data returned by these instruments will be compared with laboratory reflectance spectra to make interpretations about the surface composition of the target asteroids. Our goal in this paper is to compare spectral properties of “spectrally featureless” asteroids with new spectra of possible analogs and to supplement existing spectral libraries to support future investigation of these “featureless” asteroids.

SAMPLES AND METHODS

Samples and Preparation

Samples were loaned from the Buseck Center for Meteorite Studies (BCMS) at Arizona State University (ASU). We studied a set of aubrites, sulfide minerals, and metal-rich chondrites. The aubrites in our study are Aubres, Norton County, Mayo Belwa, Shallowater, and Khor Temiki. The sulfide mineral samples we studied are troilite (FeS), oldhamite (CaS), pyrrhotite (Fe $_{1-x}$ S), pentlandite ([Fe,Ni] $_9$ S $_8$), and a mixture of pentlandite and chalcopyrite (CuFeS $_2$). We also measured spectra from five metal-rich chondrites: the CB chondrites Isheyevo, Quebrada Chimborazo 001, Hammadah al Hamra 237, and a pair of ungrouped chondrites, Northwest Africa 5492 and Northwest Africa 12273. Characteristics of each sample studied, including name, physical form, the viewing geometry (incidence angle and emission angle, i/e) of the reflectance measurements, and spectral properties are listed in Table 1. Detailed mineralogical information of the samples is provided in Table S1 in the supporting information.

It is a well-documented phenomenon that the surface roughness and grain size of materials influence

their visible to near-infrared reflectance spectra (e.g., Clark, 1999). Therefore, we acquired spectra from multiple physical forms of the samples in our study. For the aubrites, we measured pre-existing hand samples, slabs, and unsorted powders ($\sim <1$ mm). We measured sulfide samples in slab, gravel, and powder form. Powders were produced from larger samples of meteoritic and terrestrial troilite as well as for the pyrrhotite and the pentlandite/chalcopyrite samples. For the metal-rich chondrites, we measured most in slab form only except for the CH/CBb chondrite Isheyevo, of which a small piece (~ 2 cm \times 2 cm \times 5 mm) was crushed into powder. Visual inspection of the Isheyevo piece prior to crushing suggests it belonged to the metal-rich lithology. However, this is difficult to confirm because it is unknown exactly how the smaller sections of Isheyevo in the BCMS collection relate to larger samples (Garvie et al., 2017). Our ability to crush the sample manually (see next paragraph) suggests it may have come from the metal-poor lithology, but our XRD data (Fig. S1 in the supporting information) suggest that the piece of Isheyevo used for powdering in this study was indeed dominated by metal, with a large component of Mg-rich forsterite and some Fe-bearing orthopyroxene.

All powders (including the metal-rich Isheyevo slice) were made using a Chemplex stainless steel impact mortar and pestle (Chemplex catalog #850). The impact was actuated until the full sample was crushed into <1 cm fragments. The impact mortar and pestle were cleaned with ethanol and allowed to dry after each sample was comminuted. In addition to an unsorted fraction, we dry sieved powdered samples into fractions with grain sizes greater than and less than 75 μ m to explore any spectral effects that variation in grain size might cause. This grain size range was chosen as it is consistent with hypothesized grain sizes ranges for (16) Psyche (Dollfus et al., 1979; Landsman et al., 2018). Sieves were also cleaned with ethanol and allowed to dry between each sample.

Visible to Near-Infrared Spectroscopy

Spectra were acquired using an ASD FieldSpec 4 (FS4) Standard-Res spectroradiometer over the visible to shortwave infrared (350–2500 nm) wavelength range in air at a phase angle of 30° and calibrated relative to a Spectralon white reference target. This instrument has a spectral resolution of 3 nm from 350 to 1000 nm and 10 nm resolution from 1000 to 2500 nm. For the metal-rich chondrites and sulfide samples, we found that a viewing geometry of $i = 38^\circ$, $e = 8^\circ$ eliminated stray light artifacts from strong specular reflections with negligible impact on the reflectance or spectral slope.

Table 1. Physical and spectral properties of samples used in this study.

Sample name	Form, weathering grade ^a	Grain size (μm) or roughness ^b	Viewing geometry (<i>i/e</i>)	550 nm ref ^c (%)	Vis. slope (% ref./100 nm) ^d	NIR slope (% ref./100 nm) ^d	Band center (nm) ^e	Band depth (%) ^f
Aubrites								
Mayo Belwa	Hand sample, A	<i>1, no rust</i>	30/0	20.9	1.62	−2.29	906	0.42
	Powder, A	Unsorted, <1000	30/0	20.3	2.86	−0.84	875	0.85
Aubres	Slab, A/B	<i>4</i>	30/0	47.8	−0.34	−4.00	—	—
Khor Temiki	Powder, A	Unsorted, <1000	30/0	45.7	6.09	0.39	920	0.42
Norton County	Hand sample, A/B	<i>1, no rust</i>	30/0	34.8	5.36	−0.29	887	0.53
	Powder, A	Unsorted, <1000	30/0	50.3	4.59	1.74	865	1.76
Shallowater	Slab	<i>6</i>	30/0	12.9	10.40	−2.59	966	7.62
Chondrites								
NWA 5492	Slab, B	<i>3</i>	38/8	10.2	11.93	−0.65	934	5.03
(ungrouped)	Slab, B	<i>6</i>	38/8	6.5	17.31	0.07	925	5.42
Hammadah al	Slab, A	<i>3</i>	38/8	8.9	3.50	2.29	896	6.91
Hamra 237 (CBb)	Slab, A	<i>4</i>	38/8	2.8	8.16	−0.50	932	10.80
Quebrada	Slab, A	<i>4</i>	38/8	6.1	10.64	−1.86	930	10.80
Chimborazo	Slab, A	<i>6</i>	38/8	3.7	19.92	−1.46	921	18.89
001 (CBa)								
Isheyevo	Slab, A	<i>6</i>	38/8	2.8	4.90	2.73	935	1.45
(CH/CBb)	Powder, A	Unsorted, <1000	38/8	6.8	6.24	2.53	872	1.89
	Powder, A	<75	38/8	13.7	6.68	1.96	944	0.51
	Powder, A	>75	38/8	8.1	7.17	1.56	927	1.51
	Powder, A	<75	23/8	9.5	6.47	2.08	902	0.90
	Powder, A	>75	23/8	6.9	6.86	2.03	937	1.28
	Powder, A	<75	53/8	6.6	6.33	3.43	857	3.51
	Powder, A	>75	53/8	5.3	6.71	3.18	881	3.45
NWA 12273	Slab	<i>6</i>	38/8	2.1	7.47	0.38	929	16.88
(ungrouped)	Slab	<i>4</i>	38/8	5.7	5.00	−0.07	919	9.56
Sulfides								
Bushveld	Hand sample	<i>1, no rust</i>	38/8	14.7	13.02	4.50	—	—
pentlandite	Powder	Unsorted, <1000	38/8	12.5	11.44	2.72	—	—
Norton Co. CaS	Powder	Unsorted, <1000	38/8	10.7	23.09	6.32	951	22.25
Nantan FeS	Slab	<i>5</i>	38/8	9.2	12.69	5.46	—	—
	Slab	<i>3</i>	38/8	15.3	9.60	3.04	—	—
	Powder	<500	38/8	6.9	9.77	2.95	—	—
	Powder	<75	38/8	7.8	10.02	2.70	—	—
	Powder	>75	38/8	11.5	10.22	2.39	—	—
	Powder	<75	23/8	6.9	10.04	3.32	—	—
	Powder	>75	23/8	9.2	10.33	3.10	—	—
	Powder	<75	53/8	8.1	10.22	3.19	—	—
	Powder	>75	53/8	12.5	10.30	2.48	—	—
	Powder	>75	53/8	12.5	10.30	2.48	—	—
Auburn FeS	Slab	<i>5</i>	38/8	1.6	15.08	6.68	—	—
	Powder	Unsorted, <1000	38/8	6.8	12.46	3.32	—	—
	Powder	<75	38/8	10.1	11.93	3.27	—	—
	Powder	>75	38/8	9.2	11.74	2.98	—	—
Del Norte	Slab	<i>2</i>	38/8	13.0	12.03	4.73	—	—
County FeS	Powder	Unsorted, <1000	38/8	6.6	9.64	2.39	—	—
	Powder	<75	38/8	5.3	9.52	2.67	—	—
	Powder	>75	38/8	7.4	9.87	2.25	—	—
Minas gerais pyrrhotite	Powder	Unsorted, <1 cm	38/8	11.2	12.03	6.00	—	—
	Powder	<75	38/8	11.4	9.69	5.00	—	—
	Powder	>75	38/8	12.0	10.67	5.30	—	—
	Powder	<75	23/8	9.5	9.68	5.21	—	—
	Powder	>75	23/8	9.3	10.79	6.41	—	—
	Powder	<75	53/8	10.5	9.76	5.73	—	—
	Powder	>75	53/8	12.4	10.39	4.23	—	—

Table 1. *Continued.* Physical and spectral properties of samples used in this study.

Sample name	Form, weathering grade ^a	Grain size (μm) or roughness ^b	Viewing geometry (i/e)	550 nm ref ^c (%)	Vis. slope (% ref./100 nm) ^d	NIR slope (% ref./100 nm) ^d	Band center (nm) ^e	Band depth (%) ^f
Norilsk	Powder	1, no rust	38/8	4.8	21.62	6.97	861	3.70
pentlandite/ chalcopyrite	Powder	Unsorted, <1000	38/8	11.3	16.14	1.19	898	6.10
	Powder	<75	38/8	11.0	16.76	0.84	906	5.49
	Powder	>75	38/8	12.1	16.24	2.05	890	5.67
	Powder	<75	23/8	12.9	18.03	1.76	904	5.08
	Powder	>75	23/8	14.6	17.60	1.86	906	5.97
	Powder	<75	53/8	13.5	18.04	1.10	909	5.02
	Powder	>75	53/8	12.7	17.73	2.60	887	5.35

^aWeathering grades follow ANSMET “weathering” categories and are defined as A: Minor rustiness; rust haloes on metal particles and rust stains along fractures are minor. B: Moderate rustiness; large rust haloes occur on metal particles and rust stains on internal fractures are extensive. C: Severe rustiness; metal particles have been mostly stained by rust throughout. E: Evaporite minerals visible to the naked eye. Photos of meteorite samples are available in Figures S4–S13 in the supporting information.

^bSurfaces roughness values assigned as follows: (1) unprepared hand sample, (2) rough surface with saw marks, (3) 180 grit finish, (4) 600 grit finish, (5) 1200 grit finish, (6) 1-μm diamond paste finish.

^cUncertainty on reflectance is <0.001%.

^dUncertainty on slope measurement is <0.02% ref./100 nm. Plots of phase angle versus spectral slope are in Figures S15–S18 in the supporting information.

^eUncertainty on 1-μm band center is ~1 nm. However, we note a slight correlation between near-IR slope and band centers, such that strongly sloped spectra may have longer wavelength band centers. This correlation is approximately 4.5 nm per 1% of slope, so given the 1σ standard deviation in near-IR slope (~2.1%/100 nm), our band centers are likely <±10 nm from the true value (see Fig. S14 in the supporting information).

^fUncertainty on 1-μm band depth is <0.1%.

For some samples, we collected additional spectra at phase angles of 15° and 45° to explore changes in spectral properties with changing viewing geometry. We collected spectra from visibly fresh (i.e., nonweathered) surfaces of the hand samples and slabs. For hand samples and slabs, we collected spectra from at least four different orientations and then averaged them to create a “bulk” spectrum more representative of the whole sample. For hand samples, this involved collecting spectra from multiple sides of the sample, positioning visibly fresh faces of interest of the sample normal to the center axis of the FS4’s fiber optic head using stainless steel washers. For the slab samples, we translated the sample through the ~1 cm diameter footprint of the FS4 such that a raster of points was collected for each sample. For gravel and powder samples, we poured the sample into an aluminum sample cup and rotated the cup at 90° increments through a full rotation. We then emptied the powder onto weighing paper and refilled it before repeating spectral measurements, then averaged all spectra for that sample to create a representative bulk powder spectrum. All spectra of powders were measured within 15 min of comminution to minimize interaction with the ambient lab atmosphere.

From the spectral data, we measured reflectance at 550 nm, the visible and near-infrared spectral slopes, and the center and depth of an absorption features present near ~1000 nm. The visible spectral slope was

computed between 450 and 700 nm and the near-infrared slope was computed between 760 and 1200 nm. Both slopes were calculated after the spectra were normalized to 1.0 at 550 nm. To calculate band center and depth, we follow the method of Clark and Roush (1984) and Cloutis et al. (2015). First, visually estimated shoulders of any absorption feature were used to fit a straight-line continuum across the absorption feature. The continuum was removed by dividing the sample’s absolute reflectance by this continuum line. The band centers were then found by fitting a cubic polynomial to the 20 values on either side of the minimum value of the continuum-removed features. The minimum value of the cubic polynomial was taken to be the continuum-removed band center. Band depth was determined using equation 32 of Clark and Roush (1984):

$$D_b = \frac{(R_c - R_b)}{R_c},$$

where D_b is the band depth, R_c the reflectance of the continuum at the band center, and R_b the continuum-removed reflectance at the band center. This process is repeated 50 times for each absorption feature in each spectrum using a normally distributed set of shoulder wavelengths centered on the original input shoulder wavelengths with a variance of 10 nm. Band centers and depths in Table 1 are the mean of the 50 calculated

values for each absorption feature in each spectrum. Uncertainties on these values are listed in the footnotes of Table 1.

X-Ray Diffraction Analysis

Powder XRD patterns were acquired from $<75\ \mu\text{m}$ powders using a Rigaku MiniFlex 600 X-ray diffractometer equipped with a Cu-K α X-ray source, postdiffraction graphite monochromator, and automatic divergence slit system. Powders were deposited on a glass slide and wet with methanol to reduce orientation effects in the diffraction data. Methanol was then allowed to evaporate (which typically takes $<30\ \text{s}$) before the slide was inserted into the MiniFlex X-ray diffractometer. Data were acquired from 2° to $75^\circ\ 2\theta$, at 0.02° increments, and 1 min per degree. The resulting XRD patterns were analyzed using the CrystalMaker and CrystalDiffract software. We used simulated patterns of expected endmember minerals in our samples to constrain the bulk mineralogy and interpret spectral trends.

RESULTS

X-Ray Diffraction of Powdered Samples

Figures S1–S3 in the supporting information show the XRD patterns of the Isheyevo powder and sulfides in our study. The Isheyevo XRD pattern is dominated by reflections from kamacite, pyroxene, and forsterite, as expected from its mineralogical analysis (Garvie et al., 2017). Reflections in the diffractograms of the troilites confirm that our samples are indeed dominated by troilite with minor pyrrhotite, pentlandite, daubréelite, and graphite. Finally, the diffractograms of the Bushveld pentlandite and Minas Gerais pyrrhotite confirm these samples are dominated by pentlandite and pyrrhotite, respectively, while the Norilsk sample is a subequal mixture of chalcopyrite and pentlandite.

Visible to Near-Infrared Spectroscopy

The spectra of aubrites are featureless and red-sloped at visible (450–700 nm) wavelengths (Fig. 1). They exhibit variation in near-infrared (760–1200 nm) spectral slope with most spectra exhibiting a blue slope, which is consistent with published spectra of aubrites (e.g., Burbine et al., 2002; Cloutis et al., 2016; Gaffey, 1976). Despite the low Fe content of the aubrites, the strong decrease in reflectance toward UV wavelengths is characteristic of a metal-oxygen charge transfer, which are typically thousands of times stronger than absorptions caused by crystal field transitions

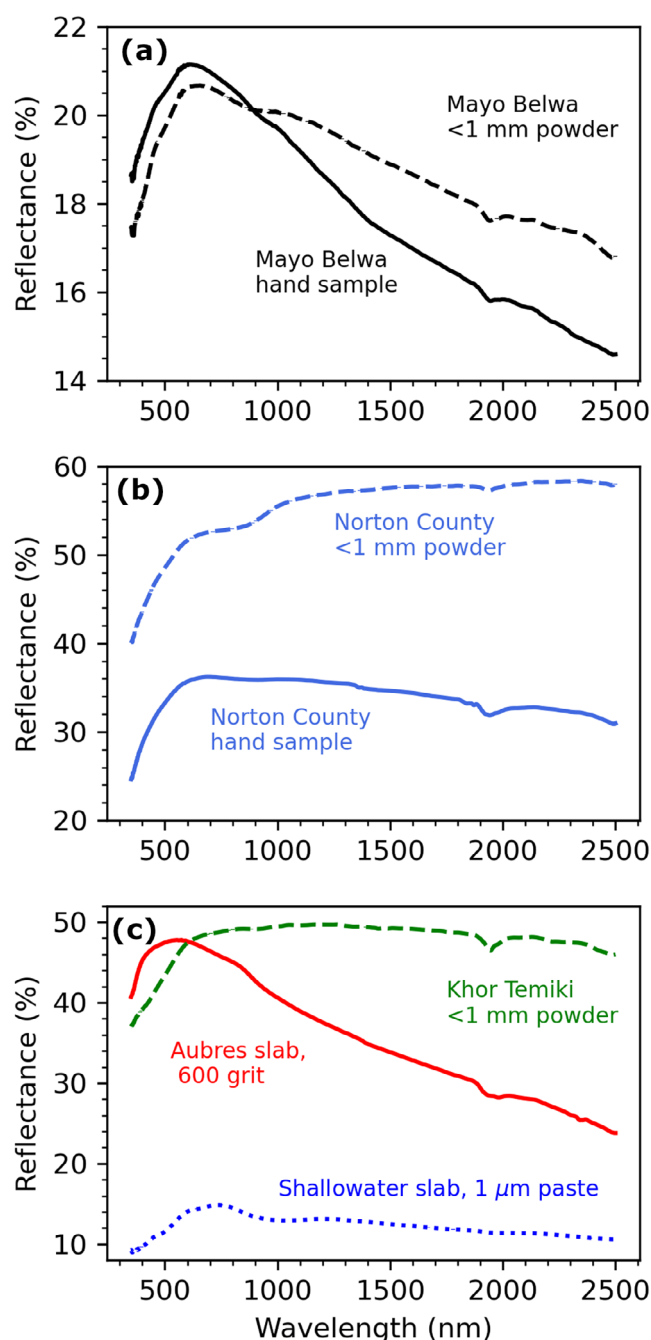


Fig. 1. Reflectance spectra of aubrite slabs and powders. A) Spectra from a hand sample (solid) and $<1\ \text{mm}$ powder (dashed) of Mayo Belwa. B) Spectra from a hand sample (solid) and $<1\ \text{mm}$ powder (dashed) of Norton County. C) Spectra from a $<1\ \text{mm}$ powder of Khor Temiki (green dashed line), a slab of Aubres (solid red line), and a slab of Shallowater (dotted blue line). (Color figure can be viewed at wileyonlinelibrary.com.)

(Clark, 1999; Gaffey, 1976). The lack of significant absorption features at $\sim 1000\ \text{nm}$ (except in the case of Shallowater) is a strong indication that pyroxene in these samples is mostly Fe-free enstatite, consistent with

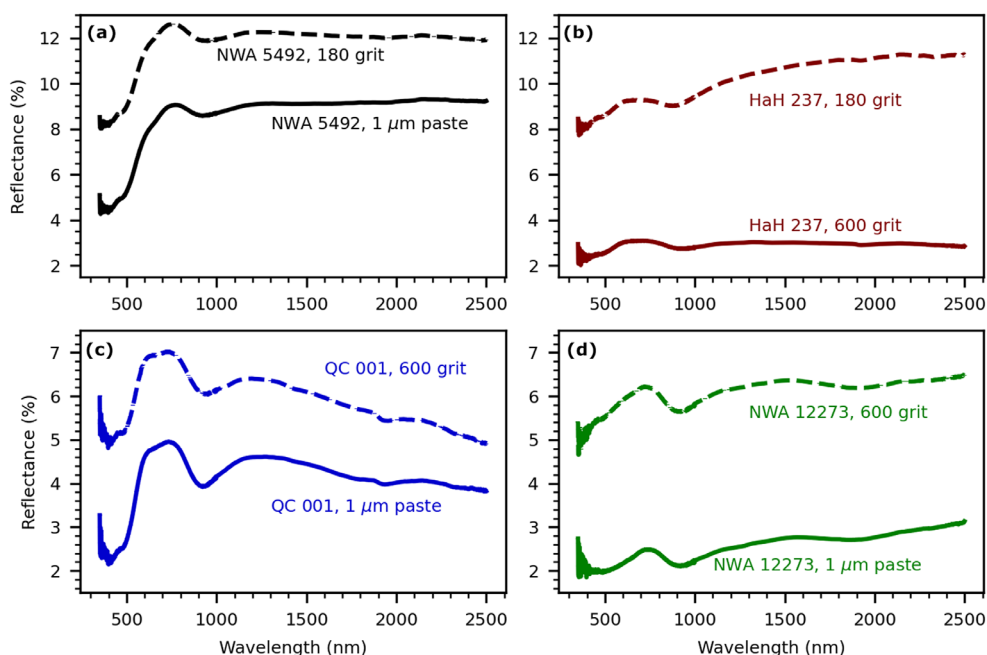


Fig. 2. Reflectance spectra of metal-rich chondrite slabs. The spectra are dark ($<15\%$ reflectance) and exhibit positive visible slopes and variable near-infrared slopes. The metal-rich chondrites in our study also generally have a subtle absorption feature at ~ 900 nm. For clarity, the finish applied to each slab is listed after the chondrite name next to each spectrum. a) Spectra from slabs of NWA 5492. b) Spectra from slabs of HaH 237. c) Spectra from slabs of QC 001. d) Spectra from NWA 12273. (Color figure can be viewed at wileyonlinelibrary.com.)

the reported mineralogy (Watters & Prinz, 1979). Shallowater, which has a higher abundance of troilite (7.1 vol%) than the other aubrites, is considerably darker (Watters & Prinz, 1979). Our aubrite spectra also exhibit subtle absorption features at ~ 1900 nm, indicative of the presence of some H_2O in the samples. Visual inspection (see photos of samples in Figs. S4–S8 in the supporting information) and the absence of additional hydroxyl features at 1400 nm indicates that our sample is not heavily rusted and likely just contains some adsorbed water (Clark, 1999). Consistent with Cloutis et al. (2016), we find that decreasing grain size (i.e., powders versus slabs) results in more red-sloped spectra for aubrites. A subtle feature at ~ 500 nm may be due to oldhamite (Cloutis et al., [2016] and Fig. 5 of this work).

Reflectance spectra of the metal-rich chondrites are generally dark ($<15\%$ reflectance) and exhibit minor absorption features at ~ 900 nm from Fe-bearing pyroxene (Figs. 2 and 3) (Adams, 1975; Gaffey, 1976). NWA 12273 exhibits a relatively significant ~ 1900 nm feature, consistent with its much higher Fe-pyroxene content. For all of the metal-rich chondrite slabs, rougher slabs exhibit higher overall reflection. HaH 237 and QC 001 exhibit a narrow absorption feature at ~ 1900 nm that, like the aubrites, is likely due to adsorbed water. NWA 5492 and QC 001 have the strongest visible slopes but lowest near-infrared slopes, while HaH 237 and NWA 12273 have more moderate visible slopes and

nearly flat near-infrared slopes. NWA 5492 has a much lower metal content than the other metal-rich chondrites (~ 20 vol% compared to >60 vol%), and thus spectra of this sample exhibit a much stronger metal-oxygen charge transfer absorption in the ultraviolet from silicates, which can result in a much steeper visible slope (Clark, 1999). A similar effect may be happening in the spectra of QC 001, which contains larger chondrules than the other samples (~ 1 cm compared to $\sim \text{mm}$), and so our method of collecting a raster of spectra across the slab surface may result in a more linear spectral mixture of silicates and metal. This areal rather than intimate mixing effect may result in an apparently stronger metal-oxygen charge transfer absorption despite the comparable bulk metal content in the sample to HaH 237 and NWA 12273. Our spectrum of NWA 12273 is darker and less red-sloped than that of Reddy et al. (2019), perhaps due to a difference in where on the surface of the sample spectra were collected.

The Isheyevo spectra are broadly consistent with a composition dominated by metal, as evidenced by red spectral slopes and a lack of strong absorption features (Fig. 3). Subtle absorption features exist at ~ 900 nm in each of the spectra, with the spectra at the highest phase angle exhibiting the largest continuum-removed band depths. Second, smaller grain sizes exhibit higher overall reflectance, consistent with a higher likelihood of multiple scattering in smaller grains (Clark, 1999). For a

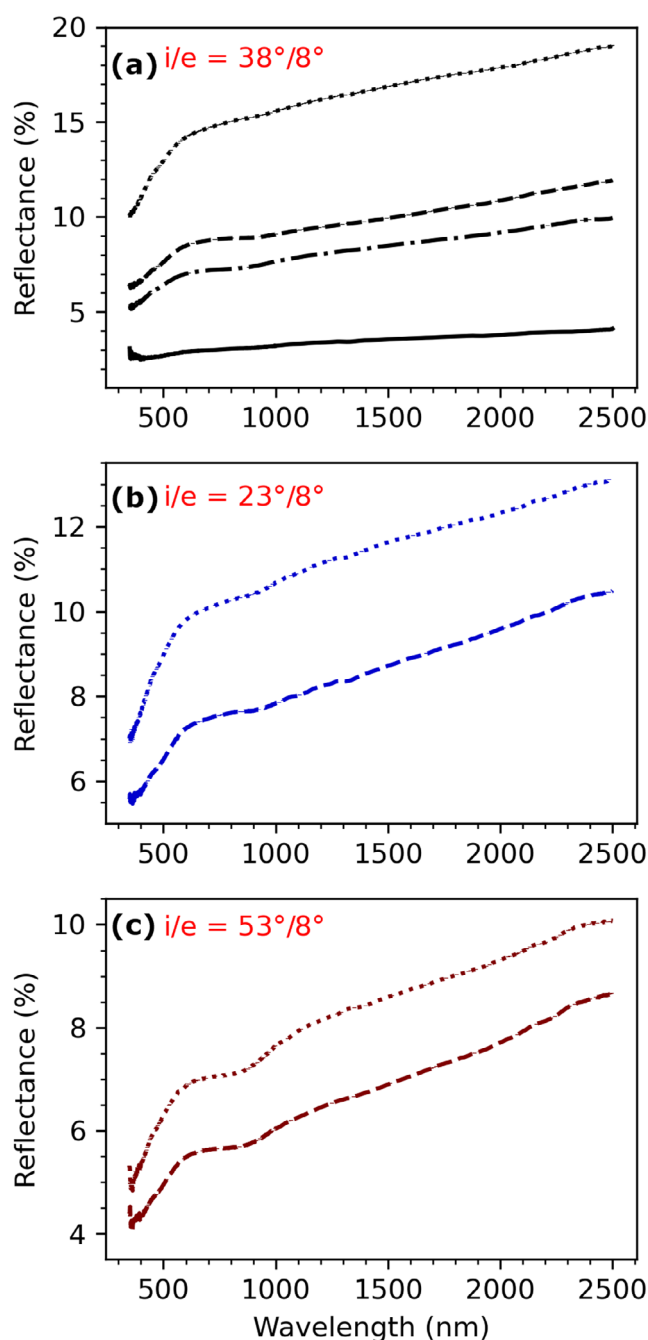


Fig. 3. Reflectance spectra of Isheyevo at different viewing geometries and grain size. a) Reflectance spectra of Isheyevo at a phase angle of 30° , (b) at 15° , and (c) at 45° . Grain size fractions are represented as: dotted = $<75\ \mu\text{m}$, dashed = $>75\ \mu\text{m}$, dashdot = unsorted, $<1\ \text{mm}$, solid = slab. (Color figure can be viewed at wileyonlinelibrary.com.)

given grain size, we find that spectra collected with a phase angle of 30° have the highest reflectance and visible slopes, while spectra collected at a phase angle of 45° have the highest near-infrared slopes and band depths. There do not appear to be any consistent trends

of the variation in band centers seen in these spectra with either grain size or phase angle.

For the Nantan troilite (Fig. 4a and 4b), the slab roughened with 180 grit paper (solid line with cross-hatching) exhibits the highest reflectance (15.3% at 550 nm), while the mixed grain size powder exhibits the lowest reflectance. Converse to the Isheyevo powder, we find that larger grain size fractions exhibit higher reflection at all phase angles. Values for visible and near-infrared slope are relatively uniform across all of the Nantan spectra, except for the smoothly polished slab, which has the highest visible slope. Spectra of the Minas Gerais pyrrhotite exhibit consistent reflectance (varying by $\sim 2.5\%$ at 550 nm) and spectral slopes across grain sizes when viewed at a 30° phase angle (Fig. 4c). The Nantan and Minas Gerais samples exhibit measurable differences in reflectance at 550 nm with increasing phase angle (Fig. 4b and 4d), contrary to the results of Varatharajan et al. (2019), who found no spectral variation at visible wavelengths in sulfides with varying viewing geometry. Spectra of the chalcopyrite–pentlandite mixture from Norilsk are shown in Fig. 4e and 4f. The hand sample of this mixture (solid line in Fig. 4e) exhibits the lowest reflectance (4.8% at 550 nm) and the highest values for both visible and near-infrared slope. Trends in spectral slope with grain size are independent of phase angle, with the larger grain size fraction always less steeply sloped at visible wavelengths and more steeply sloped at near-infrared wavelengths. Furthermore, the difference in slope at near-infrared wavelengths between grain sizes is larger with increasing phase angle. The feature at $\sim 900\ \text{nm}$ is consistent with previous measurements of chalcopyrite but may be shifted to shorter wavelengths due to the abundance of pentlandite in this sample (Vaughan & Craig, 1978). Vaughan and Craig (1978) attribute this feature to metal–metal charge transfer.

Figure 5 shows spectra of terrestrial pentlandite and oldhamite from the Norton County aubrite. The pentlandite lacks the absorption feature at $\sim 400\ \text{nm}$ found in all of our troilite spectra and the spectra of the Norilsk chalcopyrite–pentlandite mixture, indicating that this feature may be related to variations in the crystal structure caused by changes in the Fe:S ratio or the presence of Ni (Vaughan & Craig, 1978). This sample is also relatively bright compared to the other iron sulfides in our study. The visible spectral slope of oldhamite is the highest of any of the sulfides measured in our study (23.1%/100 nm). The oldhamite powder exhibits two absorption features at ~ 495 and $951\ \text{nm}$, consistent with previous measurements of oldhamite from the Norton County meteorite (Burbine et al., 2002). Studies of synthetic oldhamite typically report a single absorption feature around $400\ \text{nm}$

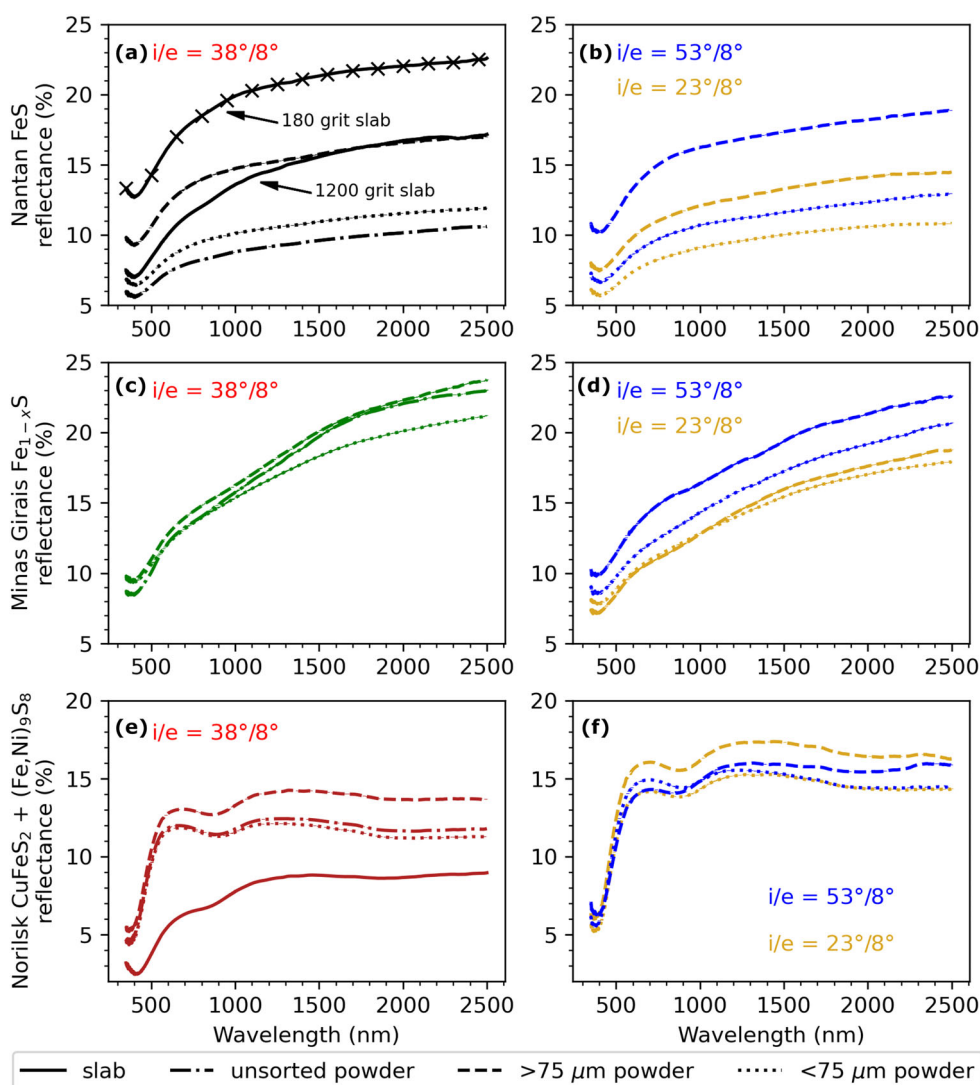


Fig. 4. Troilite from the Nantan meteorite (a, b) and pyrrhotite from Minas Gerais (c, d) are red-sloped and relatively featureless, while the mixture of chalcopyrite and pentlandite from Norilsk (e, f) have a feature at ~ 900 nm. Grain size fractions are represented as: dotted = <75 μm , dashed = >75 μm , dashdot = unsorted, <1 mm, solid = slab. The spectrum of Nantan that is solid and cross-hatched is from the 180 grit slab, while the other solid line is from a slab polished with 1200 grit paper. (Color figure can be viewed at wileyonlinelibrary.com.)

(Helbert et al., 2013; Izawa et al., 2013). Wheelock et al. (1994) measured ferromagnesian alabandite ([Fe, Mg, Mn]S; 9.7 vol%) in typical clasts of oldhamite from this meteorite with an average of 15.4 wt% Fe. While no Fe was measured in the oldhamite of Norton County by Wheelock et al. (1994), other aubrites contain oldhamite with up to several wt% Fe (Watters & Prinz, 1979). Thus, it is possible that crystal-field transitions of Fe^{2+} octahedrally coordinated with S^{2-} in either alabandite or oldhamite are the source of these two absorption features.

Figure 6 illustrates spectral differences between a meteoritic and terrestrial troilite. These samples are from the Auburn meteorite and a mine in Del Norte

County, California, respectively. Our XRD data indicate the Auburn sample is dominated by troilite with minor pyrrhotite, pentlandite, and daubréelite. Our XRD data indicate that the Del Norte sample is also dominated by troilite with minor pyrrhotite, pentlandite, and daubréelite, but also contains another mineral, likely graphite or cubanite (CuFe_2S_3).

Cloutis and Burbine (1999) noted strong variability in spectral trends between natural and synthetic troilites due to both structural and compositional variation at microscales. Our data suggest that there may be similarly significant differences between terrestrial and meteoritic troilite. For the Auburn troilite spectra, we find that smaller grain sizes result in higher overall

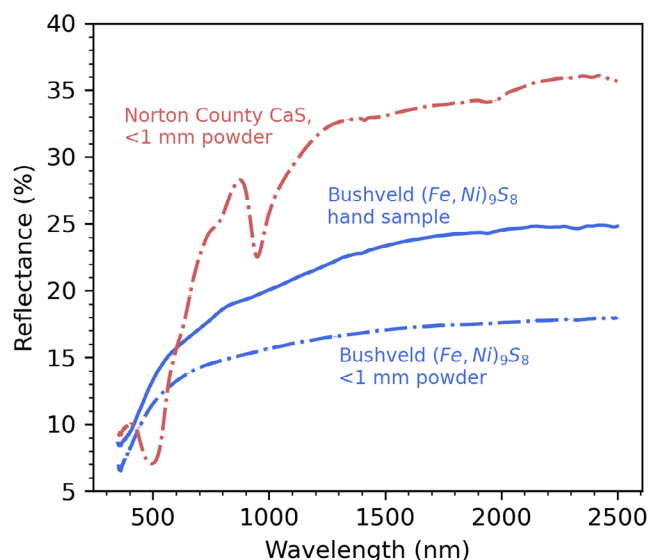


Fig. 5. Reflectance spectra of Bushveld pentlandite and Norton County oldhamite are red-sloped at both visible and near-infrared wavelengths. The oldhamite exhibits two strong absorption features at ~500 and 950 nm. (Color figure can be viewed at wileyonlinelibrary.com.)

reflectance. Conversely, the smallest grain size fraction is the darkest for the Del Norte troilite. This may be due to an unidentified, opaque mineral in the Del Norte troilite that dominates the reflectance spectrum at lower grain sizes. There is significant difference in the overall reflectance of the slab spectra between the two troilite samples. The Auburn troilite slab (polished with 1200 grit paper) is much darker than the Del Norte slab (rough cut hand sample), likely due to greater specular reflection reducing the light scattering into the fiber optic of our spectrophotometer.

DISCUSSION

Comparison to Asteroid Data

Due to their abundance and various compositional possibilities, constraining the surface compositions of “spectrally featureless” asteroids offers strong controls on our understanding of planetary formation and the current composition of the main asteroid belt. Reflectance and spectral slopes of our samples are broadly consistent with spectral properties of asteroids from “featureless” classes described in the [Introduction](#) (Fig. 7). The range of asteroid reflectance values are from the mean and standard deviations of the visible albedos for all asteroids of a particular type in the JPL Small Body Database (<https://ssd.jpl.nasa.gov/>). Asteroid spectral slopes were calculated from the mean spectrum of each asteroid type in the Bus-DeMeo taxonomy (DeMeo et al., 2009).

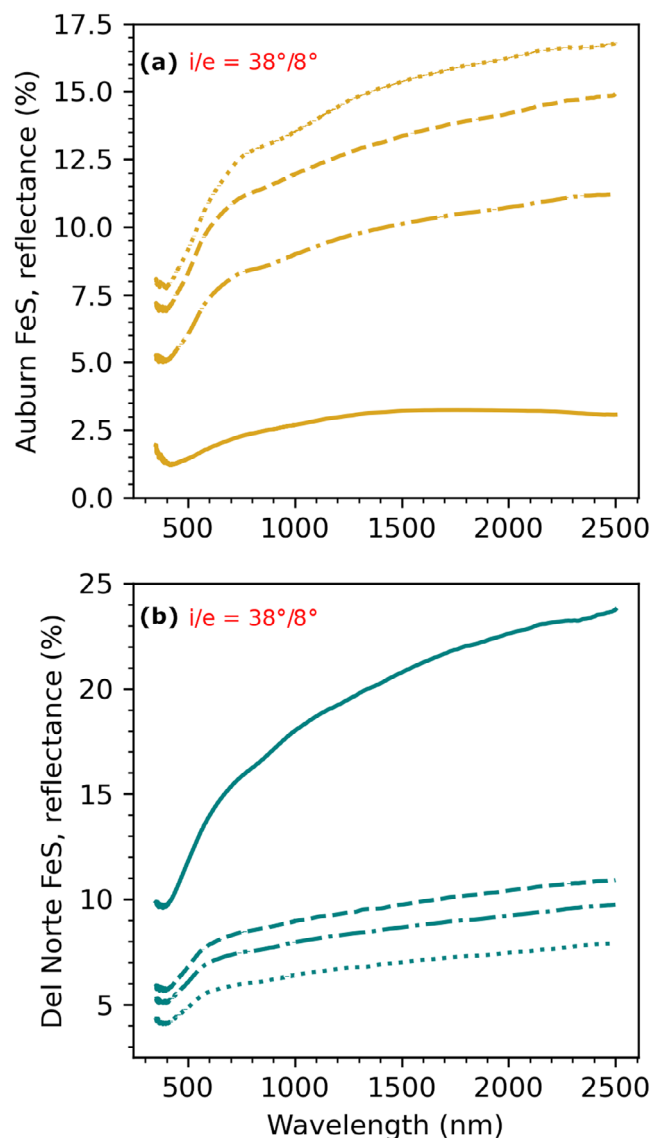


Fig. 6. Reflectance spectra of troilite from the Auburn meteorite (a) and Del Norte County, California (b). Grain size fractions are represented as: dotted = <75 μm , dashed = >75 μm , dashdot = unsorted, <1 mm, solid = slab. (Color figure can be viewed at wileyonlinelibrary.com.)

Generally, aubrites in our study have high reflectance (>20%), low-to-moderate visible slopes, and low-to-negative infrared slopes, properties most consistent with Xe-type asteroids. The connection between aubrites and the Tholen E-/Bus-DeMeo Xe-type asteroids is consistent with previous studies (Clark, Bus, Rivkin, McConnochie, et al., 2004; Fornasier et al., 2008; Gaffey & Kelley, 2004; Zellner, 1975; Zellner et al., 1977). The near-infrared slopes of our aubrites are less consistent with the range of near-infrared slopes for Xe-types, suggesting that the surfaces of these asteroids are not entirely composed of aubrite material and/or that their surfaces are being modified,

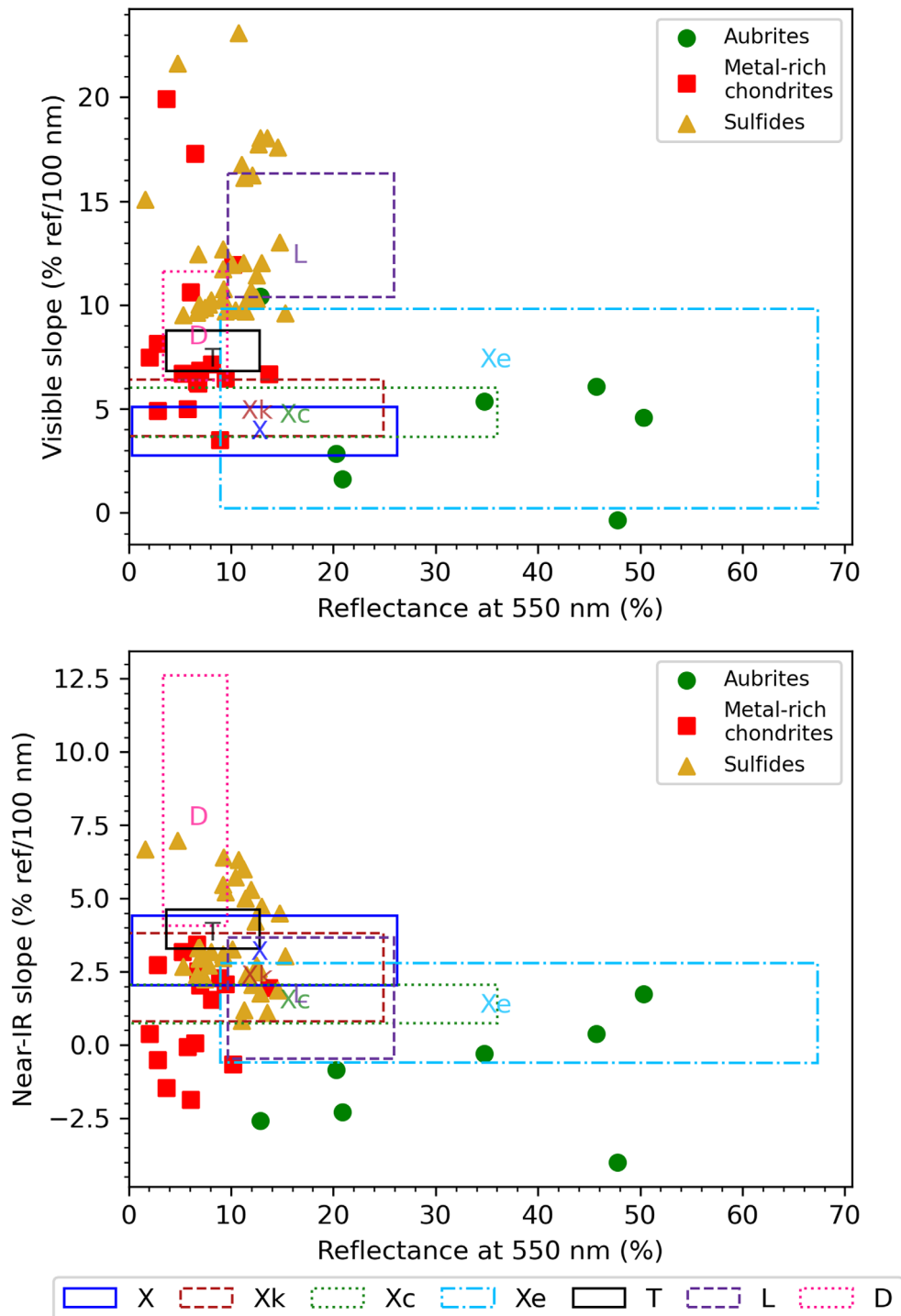


Fig. 7. Reflectance and spectral slopes of our samples are broadly consistent with albedos and spectral slopes of the “featureless” asteroid classes from the Bus-DeMeo taxonomy. Albedos for asteroids are from the JPL Small Body Database (<https://ssd.jpl.nasa.gov/>). Spectral slopes for asteroids are computed from the mean spectra in the Bus-DeMeo taxonomy (available at <http://smass.mit.edu/busdemeoclass.html>). (Color figure can be viewed at wileyonlinelibrary.com.)

possibly by space weathering. While most aubrite densities ($\sim 2.8\text{--}3.0\text{ g cm}^{-3}$) are within the range of mean densities of the Xe-type asteroids ($3.4 \pm 0.8\text{ g cm}^{-3}$), the

addition of a higher density metal (e.g., sulfides and/or metal) to the aubrites would bring both their densities and spectral properties more in line with Xe-type

asteroids (Carry, 2012; Macke et al., 2011). This interpretation that the surfaces of Xe-type asteroids may be a mixture of aubrite-like components mixed with higher density phases is consistent with measurements of the only Xe-type visited by spacecraft, (2867) Šteins (Gulkis et al., 2010; Keller et al., 2010; Leyrat et al., 2011).

Our spectra of metal-rich chondrites are consistent with published spectra of other CH and CB chondrites (e.g., Cloutis et al., 2012; Kiddell et al., 2018; Reddy et al., 2019; Trigo-Rodriguez et al., 2013) and are somewhat consistent with the X-, Xk-, and Xc-type asteroids (Fig. 7). We note that the spectra of the slabs of metal-rich chondrites fall outside of the 1σ range of the near-infrared slopes of X-, Xk-, and Xc-types, which suggests that the surfaces of these asteroids are (perhaps not surprisingly) likely not smoothly polished slabs.

A connection between metal-rich chondrites and X-type asteroids has been explored in past studies (e.g., Hardersen et al., 2011; Moyano-Camero et al., 2016). Spectral surveys of X-complex asteroids report absorption band centers ranging from ~870 to >1000 nm, consistent with the measured absorption features in our spectra of metal-rich chondrites (Clark, Bus, Rivkin, Shepard, et al., 2004; Fornasier et al., 2010; Hardersen et al., 2011). However, the band depths of the spectra from slabs of the metal-rich chondrites are significantly deeper than what has been reported for X-complex asteroids, which typically range from 1% to 3% (Clark, Bus, Rivkin, Shepard, et al., 2004; Fornasier et al., 2010; Hardersen et al., 2011). The absorption bands for the Isheyevo powders are much shallower, implying that if a metal-rich chondrite lithology is present on the surfaces of X-type asteroids, it is likely in a powder form. The high metal contents of these chondrites suggest that their densities (which are currently not measured) are consistent with the range of densities of X-, Xc-, or Xk-type asteroids (3.3 ± 2.5 , 4.0 ± 1.5 , and 4.6 ± 1.7 g cm⁻³, respectively; Carry, 2012).

Our sulfides have low to moderate reflectance (<20% at 550 nm), high visible spectral slope (>9% ref./100 nm), and a positive near-infrared spectral slope. Most of our sulfide slopes lie between ranges of reflectance and spectral slopes for the T- and L-type asteroids. There is some overlap of the reflectance and visible spectral slope of sulfides and the D-type asteroids; however, the lack of consistency between the near-infrared spectral slope of the sulfides and the D-types precludes a strong connection. Similar to our study, Britt et al. (1992), Cloutis and Gaffey (1994), and Cloutis and Burbine (1999) reported reflectance spectra of troilite that match spectra of T-type asteroids. Britt et al. (1992) hypothesized that these asteroids may be

nearly pure FeS. Despite spectral similarities, the single T-type asteroid density (2.6 ± 2.5 g cc⁻¹) reported by Carry (2012) does not strongly support an interpretation of objects dominated by solid troilite ($\rho = 4.6$ g cc⁻¹). As described in the [Bus-DeMeo D-, T-, and L-Type Asteroids and the Jupiter Trojans](#) section, L-type asteroids are categorized in the Bus-DeMeo taxonomy as occasionally having a ~2000 nm absorption feature. This feature has been hypothesized to arise from a high abundance of Fe-bearing spinel as seen in calcium-aluminum inclusions (Burbine et al., 1992; Sunshine et al., 2008). Of all the sulfide spectra presented here, only the spectrum from the mixture of chalcopyrite and pentlandite from Norilsk exhibits such a feature. While spectrally similar, the interpretation that L-type asteroids contain significant chalcopyrite (~50 vol%) would require Cu abundances significantly higher than those found in meteorites (Mittlefehldt et al., 1998; Rubin, 1997).

Asteroid (16) Psyche

Asteroid (16) Psyche is the target of the NASA Psyche Mission (Elkins-Tanton et al., 2020). Visible to near-infrared spectroscopy, radar reflectivity, thermal emissivity, and density estimates of (16) Psyche suggest it has a significant metal component (Elkins-Tanton et al., 2020; Hardersen et al., 2011; Landsman et al., 2018; Matter et al., 2013; Shepard et al., 2017). Elkins-Tanton et al. (2020) highlighted uncertainties in the bulk porosity and the nature of the nonmetal component of (16) Psyche required to resolve density estimates with compositional information from spectroscopy. Figure 8 shows the 435–2475 nm reflectance spectrum of (16) Psyche from the SMASS scaled to its Infrared Astronomical Satellite (IRAS) albedo (0.1203) at 550 nm (DeMeo et al., 2009; Tedesco et al., 2002). The spectrum of (16) Psyche is red-sloped and exhibits a subtle absorption feature centered at ~900 nm suggesting the presence of a low abundance of Fe-bearing pyroxene on the surface. Reported band centers for (16) Psyche range from 913 to 950 nm while reported band depths range from ~0% to 2.9% (Fornasier et al., 2010; Hardersen et al., 2011; Ockert-Bell et al., 2010; Sanchez et al., 2017). This range of band centers is consistent with a wide range of possible pyroxene chemistries (Adams, 1975; Cloutis & Gaffey, 1991; Horgan et al., 2014; Klima et al., 2007). An apparent absorption feature at ~1300 nm in the spectrum of (16) Psyche in Fig. 8 is likely a combination of imperfect correction of atmospheric water vapor absorption at ~1400 nm coupled with variation in the throughput of the SpeX instrument with which these data were collected (DeMeo et al., 2009;

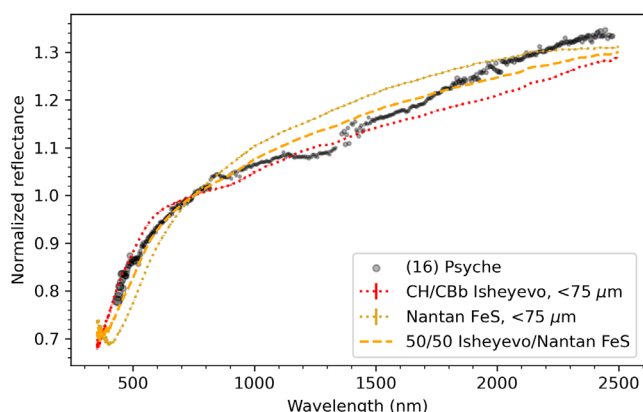


Fig. 8. The reflectance spectrum of (16) Psyche exhibits similar spectral slopes to spectra of <75 μm powder of CH/CBb chondrite Isheyevo and <75 μm powder of Nantan troilite. The laboratory spectra were acquired at a phase angle of 15° . A modeled linear mixture of the Isheyevo and Nantan troilite powder spectra is shown as a dashed line. Data for (16) Psyche are from the SMASS (DeMeo et al., 2009), collected at a solar phase angle of $\sim 13.5^\circ$. All spectra are normalized to 1.0 at 750 nm. (Color figure can be viewed at wileyonlinelibrary.com.)

Rayner et al., 2003). This ~ 1300 nm feature is not observed in other measured spectra of (16) Psyche (e.g., Fornasier et al., 2010; Hardersen et al., 2011; Ockert-Bell et al., 2010; Sanchez et al., 2017).

Figure 8 also shows reflectance spectra of <75 μm powder of the CH/CBb chondrite Isheyevo and <75 μm powder of the Nantan troilite, as well as a modeled linear 50/50 mixture of the two materials. The reflectance spectra of the endmembers exhibit similar spectral slopes to (16) Psyche, while their 550 nm reflectance are slightly less than the asteroid's IRAS albedo (9.5% and 6.9%, respectively). The modeled mixture spectrum is also visually consistent with the SMASS data of (16) Psyche. We note that the data of (16) Psyche shown in Fig. 8 are not photometrically corrected and this could be the cause of the slight differences in reflectance at 550 nm of our samples and the asteroid's albedo. While these three spectra are broadly consistent with (16) Psyche's spectrum, the spectrum of the Isheyevo powder exhibits the closest match for the ~ 900 nm absorption feature in Psyche's spectrum (Table 1; Figs. 3 and 8). The difference in spectral curvature at ~ 600 nm between the spectrum of (16) Psyche and the Isheyevo powder may be due to differences in the strength of the near-UV absorption feature caused by metal-oxygen charge transfer in silicates (e.g., Cloutis et al., 2008). Alternatively, the difference in curvature may be due to space weathering processes acting to flatten the spectrum and reduce spectral contrast compared to the Isheyevo powder (e.g., Gaffey, 2010; Hendrix & Vilas, 2006). However,

the mechanisms by which space weathering affects spectra of metal-rich surfaces are poorly understood, so it is difficult to definitively identify the cause of the ~ 600 nm spectral curvature difference.

Both (16) Psyche and Isheyevo exhibit an absorption feature at $3\text{-}\mu\text{m}$, further supporting a mineralogical connection between the two. Absorption features in this wavelength range can arise due to the presence of hydrated silicates ($\sim 2.75\text{ }\mu\text{m}$) or H_2O ($\sim 3.1\text{ }\mu\text{m}$; Rivkin et al., 1995). Takir et al. (2019) measured a $3\text{-}\mu\text{m}$ absorption feature in the spectrum of Isheyevo with a $\sim 21\%$ band depth, attributed to FeNi metal and heavily hydrated clasts. While initial measurements of (16) Psyche at $3\text{-}\mu\text{m}$ did not reveal a significant absorption (e.g., Rivkin et al., 1995), a more recent study by Takir et al. (2017) reported an absorption feature at $3\text{-}\mu\text{m}$ that was $\sim 3.0\%$ deep. Isheyevo contains sedimentary laminations consistent with gently swept-up ejecta from a glancing blow between two planetesimals, as well as chondritic material suggestive of multiple chondrule-forming events and both aqueous and thermal alteration (Bonal et al., 2010; Garvie et al., 2017; Krot et al., 2007; Morris et al., 2015). The spectral connection between Isheyevo and (16) Psyche suggests that the asteroid may be a mechanical (areal) mixture of disparate components, some of which are pristine, undifferentiated materials. Conversely, the similarity between the spectrum of (16) Psyche and troilite supports the interpretation that at least some degree of differentiation has occurred (Elkins-Tanton et al., 2020). One intriguing possibility, represented by the mixture spectrum, is that a sulfur-rich immiscible liquid might have erupted onto the surface of a mantle-stripped planetesimal following catastrophic impacts (Elkins-Tanton et al., 2020). Large regions dominated by a metal-silicate mixture composition may therefore be distinct from areas with higher sulfur content (e.g., sulfide-rich eruptions). Such a scenario is consistent with other observed surface properties (e.g., de Kleer et al., 2021; Shepard et al., 2021) and with modeling studies demonstrating the possibility of sulfur-rich ferrovolcanism on metal-rich worlds (e.g., Johnson et al., 2020).

Testing such hypotheses for the origin and evolution of the asteroid is the objective of the Psyche Mission (Elkins-Tanton et al., 2020). The Psyche spacecraft will be equipped with a pair of multispectral imagers that will provide high spatial resolution (<20 m per pixel) panchromatic images in addition to compositional information from $\geq 80\%$ of the surface using seven narrowband filters at visible to near-infrared wavelengths (~ 400 to 1100 nm; Bell et al., 2016). The multispectral data returned by the Psyche Mission can be compared with laboratory spectra, like those presented here, to test hypotheses of the asteroid's

formation by assessing the homogeneity of metal-silicate mixing, detecting some S-bearing phases like troilite and oldhamite, and possibly discriminating between silicate minerals that may help constrain the redox conditions of (16) Psyche's formation (Bell et al., 2016).

CONCLUSIONS

The data presented here allow us to explore trends in reflectance, spectral slope, and absorption band center and depth correlated with sample composition, surface roughness/grain size, and viewing geometry. We sampled a range of compositions present in aubrites and sulfides relevant to "spectrally featureless" asteroids and present new reflectance spectra of relatively unstudied metal-rich chondrites.

- Aubrites typically exhibit high reflectance and are red-sloped at visible wavelengths, exhibit a reflectance maximum at ~600 nm, and are blue-sloped in the near-infrared. Consistent with the low-Fe content of nearly pure enstatite, aubrites typically do not exhibit a ~900 nm absorption feature.
- In all forms, the metal-rich chondrites in our study exhibit low reflectance (<15% at 550 nm). Slabs exhibit variable visible slopes depending on the metal content and chondrule size and composition. Slabs generally exhibit low-to-negative near-infrared slopes. The ~900 nm absorption features are likely a complex function of silicate mineralogy, chondrule size, and metal content.
- Sulfides generally exhibit low to moderate reflectance (<20% at 550 nm), high visible spectral slope, and positive near-infrared spectral slope. Absorption features in some sulfides could prove diagnostic of certain minerals in the spectra of some asteroids. Consistent with previous studies, we show variability in the spectral properties of troilite.
- Spectra from aubrites generally match spectra from Tholen E-/Bus-DeMeo Xe-type asteroids, although the difference in near-infrared slopes of these two classes suggests that the composition of E-/Xe-type asteroids is not completely described by aubrites.
- Spectra of slabs of metal-rich chondrites are only consistent with the albedo and visible slope of X-, Xc-, and Xk-type asteroids. Powder of the Isheyevo CH/CBb chondrite is a better match for these asteroid types, suggesting their surfaces are covered in regolith.
- Spectra of sulfide minerals are generally not consistent with a specific asteroid type but instead lie between T- and L-type asteroids when reflectance is plotted against slope.
- The reflectance spectrum of asteroid (16) Psyche is broadly consistent with spectra of the powdered

Isheyevo CH/CBb chondrite and a spectrum of one of our powdered troilites and potentially a mixture of these materials. The presence of these materials on the surface of the asteroid would offer insight into its formation. Identifying such materials on the surface of the asteroid is a primary science goal of the NASA Psyche Mission.

Acknowledgments—This study was supported by funding from NASA Psyche Mission Grant NNM16AA09C. Meteoritic samples were provided for study from the BCMS at ASU. Thanks to Dr. Timothy McCoy and the Smithsonian Institution for providing the oldhamite sample used in this study. We are extremely grateful to the reviewers who helped improve this manuscript.

Data Availability Statement—The data that support the findings of this study are openly available in the Open Science Foundation repository. The OSF Project Title is: Spectral Reflectance Variations of Aubrites, Metal-rich Meteorites, and Sulfides: Implications for Exploration of (16) Psyche and other 'Spectrally Featureless' Asteroids at <http://doi.org/10.17605/OSF.IO/7JXB3>.

Editorial Handling—Dr. Edward Anthony Cloutis

REFERENCES

- Adams, J. B. 1975. Interpretation of Visible and Near-Infrared Diffuse Reflectance Spectra of Pyroxenes and Other Rock-Forming Minerals. In *Infrared and Raman Spectroscopy of Lunar and Terrestrial Minerals*, edited by C. Karr, 91–116. New York, NY: Academic Press, Inc.
- Agee C. B., Vaci Z., Ziegler K., and Spilde M. N. 2019. Northwest Africa 12273: Unique Ungrouped Metal-Rich Chondrite (Abstract #1176). 50th Lunar and Planetary Science Conference. CD-ROM.
- Bell J., Elkins-Tanton L. T., Polanskey C. A., Ravine M. A., Caplinger M. A., Asphaug E., Bercovici D., Bills B. G., Binzel R. P., Bottke W. F., and Jaumann R. 2016. The Psyche Multispectral Imager Investigation: Characterizing the Geology, Topography, and Compositional Properties of a Metallic World (Abstract #1366). 47th Lunar and Planetary Science Conference. CD-ROM.
- Binzel, R. P., and Xu, S. 1993. Chips Off of Asteroid 4 Vesta: Evidence for the Parent Body of Basaltic Achondrite Meteorites. *Science* 260: 186–91.
- Bonal, L., Huss, G. R., Krot, A. N., Nagashima, K., Ishii, H. A., and Bradley, J. P. 2010. Highly ¹⁵N-Enriched Chondritic Clasts in the CB/CH-Like Meteorite Isheyevo. *Geochimica et Cosmochimica Acta* 74: 6590–609.
- Bradley J. P. 2003. Interplanetary Dust Particles. In *Treatise on Geochemistry*, edited by H. D. Holland and K. K. Turekian, 711–35. Amsterdam: Elsevier Science.
- Bradley, J. P., Keller, L. P., Brownlee, D. E., and Thomas, K. L. 1996. Reflectance Spectroscopy of Interplanetary Dust Particles. *Meteoritics & Planetary Science* 31: 394–402.

- Britt D. T., Bell J. F., Haack H., and Scott E. R. D. 1992. The Reflectance Spectrum of Troilite (Abstract). 23rd Lunar and Planetary Science Conference. p. 1083.
- Brown, M. E. 2016. The 3–4 μm Spectra of Jupiter Trojan Asteroids. *The Astronomical Journal* 152: 159.
- Burbine, T. H., Gaffey, M. J., and Bell, J. F. 1992. S-Asteroids 387 Aquitania and 980 Anacostia: Possible Fragments of the Breakup of a Spinel-Bearing Parent Body with C03/CV3 Affinities. *Meteoritics* 27: 424–34.
- Burbine, T. H., McCoy, T. J., Nittler, L. R., Benedix, G. K., Cloutis, E. A., and Dickinson, T. L. 2002. Spectra of Extremely Reduced Assemblages: Implications for Mercury. *Meteoritics & Planetary Science* 37: 1233–44.
- Bus, S. J., and Binzel, R. P. 2002. Phase II of the Small Main-Belt Asteroid Spectroscopic Survey: A Feature-Based Taxonomy. *Icarus* 158: 146–77.
- Carry, B. 2012. Density of Asteroids. *Planetary and Space Science* 73: 98–118.
- Clark, B. E., Bus, S. J., Rivkin, A. S., McConnochie, T., Sanders, J., Shah, S., Hiroi, T., and Shepard, M. 2004. E-Type Asteroid Spectroscopy and Compositional Modeling. *Journal of Geophysical Research: Planets* 109: 1–11.
- Clark, B. E., Bus, S. J., Rivkin, A. S., Shepard, M. K., and Shah, S. 2004. Spectroscopy of X-Type Asteroids. *The Astronomical Journal* 128: 3070–81.
- Clark, B. E., Veverka, J., Helfenstein, P., Thomas, P. C., Bell, J. F. III, Harch, A., Robinson, M. S., Murchie, S. L., McFadden, L. A., and Chapman, C. R. 1999. NEAR Photometry of Asteroid 253 Mathilde. *Icarus* 140: 53–65.
- Clark, R. N. 1999. Spectroscopy of Rocks and Minerals, and Principles of Spectroscopy. In *Manual of Remote Sensing*, edited by A. N. Rencz, 3rd ed., 3–58. New York, NY: John Wiley & Sons.
- Clark, R. N., and Roush, T. L. 1984. Reflectance Spectroscopy: Quantitative Analysis Techniques for Remote Sensing Applications. *Journal of Geophysical Research: Solid Earth* 89: 6329–40.
- Cloutis E. A., and Burbine T. H. 1999. The Spectral Properties of Troilite/Pyrrhotite and Implications for the E-Asteroids (Abstract #1875). 30th Lunar and Planetary Science Conference. CD-ROM.
- Cloutis, E. A., and Gaffey, M. J. 1991. Pyroxene Spectroscopy Revisited: Spectral-Compositional Correlations and Relationship to Geothermometry. *Journal of Geophysical Research: Planets* 96: 22809–26.
- Cloutis E. A., and Gaffey M. J. 1994. An X-Ray Diffraction and Reflectance Spectroscopy Study of Iron Sulphides (Abstract). 25th Lunar and Planetary Science Conference. p. 273.
- Cloutis E. A., Gaffey M. J., and Applin D. M. 2016. Spectral Reflectance Properties of Aubrites (Abstract #1709). 47th Lunar and Planetary Science Conference. CD-ROM.
- Cloutis, E. A., Gaffey, M. J., Smith, D. G., and Lambert, R. S. J. 1990. Reflectance Spectra of “Featureless” Materials and the Surface Mineralogies of M- and E-Class Asteroids. *Journal of Geophysical Research: Solid Earth* 95: 281–93.
- Cloutis, E. A., Hudon, P., Hiroi, T., Gaffey, M. J., and Mann, P. 2012. Spectral Reflectance Properties of Carbonaceous Chondrites: 8. “Other” Carbonaceous Chondrites: CH, Ungrouped, Polymict, Xenolithic Inclusions, and R Chondrites. *Icarus* 221: 984–1001.
- Cloutis, E. A., McCormack, K. A., Bell, J. F. III, Hendrix, A. R., Bailey, D. T., Craig, M. A., Mertzman, S. A., Robinson, M. S., and Riner, M. A. 2008. Ultraviolet Spectral Reflectance Properties of Common Planetary Minerals. *Icarus* 197: 321–47.
- Cloutis, E. A., Sanchez, J. A., Reddy, V., Gaffey, M. J., Binzel, R. P., Burbine, T. H., Hardersen, P. S., et al. 2015. Olivine–Metal Mixtures: Spectral Reflectance Properties and Application to Asteroid Reflectance Spectra. *Icarus* 252: 39–82.
- Coradini, A., Capaccioni, F., Erard, S., Arnold, G., De Sanctis, M. C., Filacchione, G., Tosi, F., et al. 2011. The Surface Composition and Temperature of Asteroid 21 Lutetia as Observed by Rosetta/VIRTIS. *Science* 334: 492–4.
- DeMeo, F. E., Binzel, R. P., Slivan, S. M., and Bus, S. J. 2009. An Extension of the Bus Asteroid Taxonomy into the Near-Infrared. *Icarus* 202: 160–80.
- Devog le, M., Tanga, P., Cellino, A., Bendjoya, P., Rivet, J. P., Surdej, J., Vernet, D., et al. 2018. New Polarimetric and Spectroscopic Evidence of Anomalous Enrichment in Spinel-Bearing Calcium-Aluminium-Rich Inclusions Among L-Type Asteroids. *Icarus* 304: 31–57.
- Dollfus, A., Mandeville, J. C., and Duseaux, M. 1979. The Nature of the M-Type Asteroids from Optical Polarimetry. *Icarus* 37: 124–32.
- Elkins-Tanton, L. T., Asphaug, E., Bell, J. F. III, Bercovici, H., Bills, B., Binzel, R., Bottke, W. F., et al. 2020. Observations, Meteorites, and Models: A Preflight Assessment of the Composition and Formation of (16) Psyche. *Journal of Geophysical Research: Planets* 125: e2019JE006296.
- Emery, J. P., and Brown, R. H. 2003. Constraints on the Surface Composition of Trojan Asteroids from Near-Infrared (0.8–4.0 μm) Spectroscopy. *Icarus* 164: 104–21.
- Emery, J. P., Burr, D. M., and Cruikshank, D. P. 2011. Near-Infrared Spectroscopy of Trojan Asteroids: Evidence for Two Compositional Groups. *The Astronomical Journal* 141: 25.
- Emery, J. P., Marzari, F., Morbidelli, A., French, L. M., and Grav, T. 2015. The Complex History of Trojan Asteroids. *Asteroids IV* 203–220.
- Ferrari, F., Franzese, V., Pugliatti, M., Giordano, C., and Toppoto, F. 2021. Preliminary Mission Profile of Hera’s Milani CubeSat. *Advances in Space Research* 67: 2010–29.
- Fornasier, S., Clark, B. E., Dotto, E., Migliorini, A., Ockert-Bell, M., and Barucci, M. A. 2010. Spectroscopic Survey of M-type Asteroids. *Icarus* 210: 655–73.
- Fornasier, S., Lantz, C., Barucci, M. A., and Lazzarin, M. 2014. Aqueous Alteration on Main Belt Primitive Asteroids: Results from Visible Spectroscopy. *Icarus* 233: 163–78.
- Fornasier, S., Migliorini, A., Dotto, E., and Barucci, M. A. 2008. Visible and Near Infrared Spectroscopic Investigation of E-type Asteroids, Including 2867 Steins, a Target of the Rosetta Mission. *Icarus* 196: 119–34.
- Friend P., Zipfel J., Gellissen M., Kleinschrodt R., Muenker C., Pack A., Schulz T., Stracke A., and Palme H. 2011. Northwest Africa 5492: An Extremely Reduced Chondritic Meteorite with Low Volatile Element Contents (Abstract #1095). 42nd Lunar and Planetary Science Conference. CD-ROM.
- F ri, E., and Marty, B. 2015. Nitrogen Isotope Variations in the Solar System. *Nature Geoscience* 8: 515–22.
- Gaffey, M. J. 1976. Spectral Reflectance Characteristics of the Meteorite Classes. *Journal of Geophysical Research* 81: 905–20.

- Gaffey, M. J. 2010. Space Weathering and the Interpretation of Asteroid Reflectance Spectra. *Icarus* 209: 564–74.
- Gaffey M. J. and Kelley M. S. 2004. Mineralogical Variations Among High Albedo E-Type Asteroids: Implications for Asteroid Igneous Processes (Abstract #1812). 35th Lunar and Planetary Science Conference. CD-ROM.
- Garvie, L. A., Knauth, L. P., and Morris, M. A. 2017. Sedimentary Laminations in the Isheyevo (CH/CBb) Carbonaceous Chondrite Formed by Gentle Impact-Plume Sweep-Up. *Icarus* 292: 36–47.
- Gulkis, S., Keihm, S., Kamp, L., Backus, C., Janssen, M., Lee, S., Davidsson, B., et al. 2010. Millimeter and Submillimeter Measurements of Asteroid (2867) Steins During the Rosetta Fly-By. *Planetary and Space Science* 58: 1077–87.
- Hanuš, J., Viikinkoski, M., Marchis, F., Ďurech, J., Kaasalainen, M., Delbo, M., Herald, D., et al. 2017. Volumes and Bulk Densities of Forty Asteroids from ADAM Shape Modeling. *Astronomy & Astrophysics* 601: A114–55.
- Hardersen, P. S., Cloutis, E. A., Reddy, V., Mothé-Diniz, T., and Emery, J. P. 2011. The M-/X-Asteroid Menagerie: Results of an NIR Spectral Survey of 45 Main-Belt Asteroids. *Meteoritics & Planetary Science* 46: 1910–38.
- Helbert, J., Maturilli, A., and D'Amore, M. 2013. Visible and Near-Infrared Reflectance Spectra of Thermally Processed Synthetic Sulfides as a Potential Analog for the Hollow Forming Materials on Mercury. *Earth and Planetary Science Letters* 369: 233–8.
- Hendrix, A. R., and Vilas, F. 2006. The Effects of Space Weathering at UV Wavelengths: S-Class Asteroids. *The Astronomical Journal* 132: 1396.
- Hiroi T., Pieters C. M., Rutherford M. J., Zolensky M. E., Sasaki S., Ueda Y., and Miyamoto M. 2004. What are the P-Type Asteroids Made of? (Abstract #1616) 35th Lunar and Planetary Science Conference. CD-ROM.
- Hiroi, T., Zolensky, M. E., and Pieters, C. M. 2001. The Tagish Lake Meteorite: A Possible Sample from a D-Type Asteroid. *Science* 293: 2234–6.
- Horgan, B. H., Cloutis, E. A., Mann, P., and Bell, J. F. III. 2014. Near-Infrared Spectra of Ferrous Mineral Mixtures and Methods for Their Identification in Planetary Surface Spectra. *Icarus* 234: 132–54.
- Ivanova M. A., Kononkova N. N., Franchi I. A., Verchovsky A. B., Korochantseva E. V., Trieloff M., Krot A. N., and Brandstätter F. 2006. Isheyevo Meteorite: Genetic Link Between CH and CB Chondrites? (Abstract #1100). 37th Lunar and Planetary Science Conference. CD-ROM.
- Ivanova, M. A., Kononkova, N. N., Krot, A. N., Greenwood, R. C., Franchi, I. A., Verchovsky, A. B., Trieloff, M., Korochantseva, E. V., and Brandstätter, F. 2008. The Isheyevo Meteorite: Mineralogy, Petrology, Bulk Chemistry, Oxygen, Nitrogen, Carbon Isotopic Compositions, and ^{40}Ar - ^{39}Ar Ages. *Meteoritics & Planetary Science* 43: 915–40.
- Izawa, M. R., Flemming, R. L., King, P. L., Peterson, R. C., and McCausland, P. J. 2010. Mineralogical and Spectroscopic Investigation of the Tagish Lake Carbonaceous Chondrite by X-Ray Diffraction and Infrared Reflectance Spectroscopy. *Meteoritics & Planetary Science* 45: 675–98.
- Izawa, M. R. M., Applin, D. M., Mann, P., Craig, M. A., Cloutis, E. A., Helbert, J., and Maturilli, A. 2013. Reflectance Spectroscopy (200–2500 nm) of Highly-Reduced Phases Under Oxygen- and Water-Free Conditions. *Icarus* 226: 1612–7.
- Johnson, B. C., Sori, M. M., and Evans, A. J. 2020. Ferrovolcanism on Metal Worlds and the Origin of Pallasites. *Nature Astronomy* 4: 41–4.
- Jones, T. D., Lebofsky, L. A., Lewis, J. S., and Marley, M. S. 1990. The Composition and Origin of the C, P, and D Asteroids: Water as a Tracer of Thermal Evolution in the Outer Belt. *Icarus* 88: 172–92.
- Keil, K. 2010. Enstatite Achondrite Meteorites (Aubrites) and the Histories of Their Asteroidal Parent Bodies. *Geochemistry* 70: 295–317.
- Keller, H. U., Barbieri, C., Koschny, D., Lamy, P., Rickman, H., Rodrigo, R., Sierks, H., et al. 2010. E-Type Asteroid (2867) Steins as Imaged by OSIRIS on Board Rosetta. *Science* 327: 190–3.
- Kiddell, C. B., Cloutis, E. A., Dagdick, B. R., Stromberg, J. M., Applin, D. M., and Mann, J. P. 2018. Spectral Reflectance of Powder Coatings on Carbonaceous Chondrite Slabs: Implications for Asteroid Regolith Observations. *Journal of Geophysical Research: Planets* 123: 2803–40.
- de Kleer, K., Cambioni, S., and Shepard, M. 2021. The Surface of (16) Psyche from Thermal Emission and Polarization Mapping. *The Planetary Science Journal* 2: 149.
- Klima, R. L., Pieters, C. M., and Dyar, M. D. 2007. Spectroscopy of Synthetic Mg-Fe Pyroxenes I: Spin-Allowed and Spin-Forbidden Crystal Field Bands in the Visible and Near-Infrared. *Meteoritics & Planetary Science* 42: 235–53.
- Koch T. E., Brenker F. E., Krot A. N., and Bizzarro M. 2016. Petrography of Quebrada Chimborazo 001—A New CBA Chondrite (Abstract #1968). 47th Lunar and Planetary Science Conference. CD-ROM.
- Krot, A. N., Ivanova, M. A., and Ulyanov, A. A. 2007. Chondrules in the CB/CH-Like Carbonaceous Chondrite Isheyevo: Evidence for Various Chondrule-Forming Mechanisms and Multiple Chondrule Generations. *Geochemistry* 67: 283–300.
- Krot, A. N., Ulyanov, A. A., and Ivanova, M. A. 2008. Refractory Inclusions in the CH/CB-Like Carbonaceous Chondrite Isheyevo: I. Mineralogy and Petrography. *Meteoritics & Planetary Science* 43: 1531–50.
- Landsman, Z. A., Emery, J. P., Campins, H., Hanuš, J., Lim, L. F., and Cruikshank, D. P. 2018. Asteroid (16) Psyche: Evidence for a Silicate Regolith from Spitzer Space Telescope Spectroscopy. *Icarus* 304: 58–73.
- Lebofsky, L. A., Jones, T. D., Owensby, P. D., Feierberg, M. A., and Consolmagno, G. J. 1990. The Nature of Low-Albedo Asteroids from 3- μm Multi-Color Photometry. *Icarus* 83: 16–26.
- Levison H. F. and the Lucy Science Team. 2016. Lucy: Surveying the Diversity of the Trojan Asteroids, the Fossils of Planet Formation (Abstract #2061). 47th Lunar and Planetary Science Conference. CD-ROM.
- Leyrat, C., Coradini, A., Erard, S., Capaccioni, F., Capria, M. T., Drossart, P., De Sanctis, M. C., Tosi, F., and VIRTIS Team. 2011. Thermal Properties of the Asteroid (2867) Steins as Observed by VIRTIS/Rosetta. *Astronomy & Astrophysics* 531: A168.
- Macke, R. J., Britt, D. T., and Consolmagno, G. J. 2011. Density, Porosity, and Magnetic Susceptibility of Achondritic Meteorites. *Meteoritics & Planetary Science* 46: 311–26.

- Matter, A., Delbo, M., Carry, B., and Ligorì, S. 2013. Evidence of a Metal-Rich Surface for the Asteroid (16) Psyche from Interferometric Observations in the Thermal Infrared. *Icarus* 226: 419–27.
- Meibom, A., Richter, K., Chabot, N., Dehn, G., Antignano, A., McCoy, T. J., Krot, A. N., Zolensky, M. E., Petaev, M. I., and Keil, K. 2005. Shock Melts in QUE 94411, Hammadah al Hamra 237, and Bencubbin: Remains of the Missing Matrix? *Meteoritics & Planetary Science* 40: 1377–91.
- Mittlefehldt, D. W., McCoy, T. J., Goodrich, C. A., and Kracher, A. 1998. Non-Chondritic Meteorites from Asteroidal Bodies. In *Planetary Materials*, edited by J. J. Papike, 523–718. Albuquerque, New Mexico: De Gruyter.
- Morris, M. A., Garvie, L. A., and Knauth, L. P. 2015. New Insight into the Solar System's Transition Disk Phase Provided by the Metal-Rich Carbonaceous Chondrite Isheyevo. *The Astrophysical Journal Letters* 801: L22.
- Moyano-Camero, C. E., Trigo-Rodríguez, J. M., Llorca, J., Fornasier, S., Barucci, M. A., and Rimola, A. 2016. A Plausible Link Between the Asteroid 21 Lutetia and CH Carbonaceous Chondrites. *Meteoritics & Planetary Science* 51: 1795–812.
- Ockert-Bell, M. E., Clark, B. E., Shepard, M. K., Isaacs, R. A., Cloutis, E. A., Fornasier, S., and Bus, S. J. 2010. The Composition of M-Type Asteroids: Synthesis of Spectroscopic and Radar Observations. *Icarus* 210: 674–92.
- Rayner, J. T., Toomey, D. W., Onaka, P. M., Denault, A. J., Stahlberger, W. E., Vacca, W. D., Cushing, M. C., and Wang, S. 2003. SpeX: A Medium-Resolution 0.8–5.5 Micron Spectrograph and Imager for the NASA Infrared Telescope Facility. *Publications of the Astronomical Society of the Pacific* 115: 362.
- Reddy V., Pearson N., Agee C. B., Cantillo D. C., Le Corre L., Campbell T., and Chabra O. 2019. Spectral Investigation of Anomalous Metal-Rich Chondrite Northwest Africa (NWA) 12273: Implications for Asteroid (16) Psyche (Abstract #2212). 50th Lunar and Planetary Science Conference. CD-ROM.
- Rivkin, A. S., Howell, E. S., Britt, D. T., Lebofsky, L. A., Nolan, M. C., and Branstetter, D. D. 1995. 3- μ m Spectrophotometric Survey of M- and E-Class Asteroids. *Icarus* 117: 90–100.
- Rivkin, A. S., Howell, E. S., Lebofsky, L. A., Clark, B. E., and Britt, D. T. 2000. The Nature of M-Class Asteroids from 3- μ m Observations. *Icarus* 145: 351–68.
- Rivkin, A. S., Howell, E. S., Vilas, F., and Lebofsky, L. A. 2002. Hydrated Minerals on Asteroids: The Astronomical Record. In *Asteroids III*, edited by W. F. Bottke, A. Cellino, P. Paolicchi, and R. P. Binzel, 235–53. Tucson, Arizona: University of Arizona Press.
- Rubin, A. E. 1997. Mineralogy of Meteorite Groups. *Meteoritics & Planetary Science* 32: 231–47.
- Sanchez, J. A., Reddy, V., Shepard, M. K., Thomas, C., Cloutis, E. A., Takir, D., Conrad, A., Kiddell, C., and Applin, D. 2017. Detection of Rotational Spectral Variation on the M-Type Asteroid (16) Psyche. *The Astronomical Journal* 153: 29–37.
- Shepard, M. K., de, Kleer, K., Cambioni, S., Taylor, P. A., Virkki, A. K., Rivera-Valentin, E. G., Sanchez-Vahamonde, C. R., et al. 2021. Asteroid 16 Psyche: Shape, Features, and Global Map. *The Planetary Science Journal* 2: 125.
- Shepard, M. K., Richardson, J., Taylor, P. A., Rodriguez-Ford, L. A., Conrad, A., de, Pater, I., Adamkovics, M., et al. 2017. Radar Observations and Shape Model of Asteroid 16 Psyche. *Icarus* 281: 388–403.
- Shepard, M. K., Taylor, P. A., Nolan, M. C., Howell, E. S., Springmann, A., Giorgini, J. D., Warner, B. D., et al. 2015. A Radar Survey of M- and X-Class Asteroids. III. Insights into Their Composition, Hydration State, & Structure. *Icarus* 245: 38–55.
- Sunshine, J. M., Connolly, H. C., McCoy, T. J., Bus, S. J., and La Croix, L. M. 2008. Ancient Asteroids Enriched in Refractory Inclusions. *Science* 320: 514–7.
- Takir, D., and Emery, J. P. 2012. Outer Main Belt Asteroids: Identification and Distribution of four 3- μ m Spectral Groups. *Icarus* 219: 641–54.
- Takir, D., Reddy, V., Sanchez, J. A., Shepard, M. K., and Emery, J. P. 2017. Detection of Water and/or Hydroxyl on Asteroid (16) Psyche. *The Astronomical Journal* 153: 31.
- Takir, D., Stockstill-Cahill, K. R., Hibbitts, C. A., and Nakauchi, Y. 2019. 3- μ m Reflectance Spectroscopy of Carbonaceous Chondrites Under Asteroid-Like Conditions. *Icarus* 333: 243–51.
- Tedesco, E. F., Noah, P. V., Noah, M., and Price, S. D. 2002. The Supplemental IRAS Minor Planet Survey. *The Astronomical Journal* 123: 1056–85.
- Tholen D. J. 1984. Asteroid Taxonomy from Cluster Analysis of Photometry. PhD thesis, University of Arizona, Tucson, Arizona.
- Trigo-Rodríguez, J. M., Moyano-Camero, C. E., Llorca, J., Fornasier, S., Barucci, M. A., Belskaya, I., Martins, Z., et al. 2013. UV to Far-IR Reflectance Spectra of Carbonaceous Chondrites—I. Implications for Remote Characterization of Dark Primitive Asteroids Targeted by Sample-Return Missions. *Monthly Notices of the Royal Astronomical Society* 437: 227–40.
- Varatharajan, I., Maturilli, A., Helbert, J., Alemanno, G., and Hiesinger, H. 2019. Spectral Behavior of Sulfides in Simulated Daytime Surface Conditions of Mercury: Supporting Past (MESSENGER) and Future Missions (BepiColombo). *Earth and Planetary Science Letters* 520: 127–40.
- Vaughan D. J., and Craig J. R. 1978. *Mineral Chemistry of Metal Sulfides*. Cambridge: Cambridge University Press.
- Vernazza, P., Marsset, M., Beck, P., Binzel, R. P., Birlan, M., Brunetto, R., Demeo, F. E., et al. 2015. Interplanetary Dust Particles as Samples of Icy Asteroids. *The Astrophysical Journal* 806: 204–14.
- Watters T. R., and Prinz M. 1979. Aubrites—Their Origin and Relationship to Enstatite Chondrites (Abstract). 10th Lunar and Planetary Science Conference. pp. 1073–93.
- Weisberg, M. K., Bunch, T. E., Wittke, J. H., Rumble, D. III, and Ebel, D. S. 2012. Petrology and Oxygen Isotopes of NWA 5492, a New Metal-Rich Chondrite. *Meteoritics & Planetary Science* 47: 363–73.
- Weisberg, M. K., Prinz, M., Clayton, R. N., Mayeda, T. K., Sugiura, N., and Zashu, S. 1998. The Bencubbinite (B) Group of the CR Clan. *Meteoritics & Planetary Science Supplement* 33: A166.
- Wheelock, M. M., Keil, K., Floss, C., Taylor, G. J., and Crozaz, G. 1994. REE Geochemistry of Oldhamite-Dominated Clasts from the Norton County Aubrite: Igneous Origin of Oldhamite. *Geochimica et Cosmochimica Acta* 58: 449–58.
- Zellner, B. 1975. 44 NYSA—An Iron-Depleted Asteroid. *The Astrophysical Journal* 198: L45–7.

- Zellner, B., Leake, M., Morrison, D., and Williams, J. G. 1977. The E Asteroids and the Origin of the Enstatite Achondrites. *Geochimica et Cosmochimica Acta* 41: 1759–67.
- Zellner, B., Tholen, D. J., and Tedesco, E. F. 1985. The Eight-Color Asteroid Survey: Results for 589 Minor Planets. *Icarus* 61: 355–416.
- Zipfel J., Wlotzka F., and Spettel B. 1998. Bulk Chemistry and Mineralogy of a New "Unique" Metal-Rich Chondritic Breccia, Hammadah al Hamra 237 (Abstract #1417). 29th Lunar and Planetary Science Conference. CD-ROM.

SUPPORTING INFORMATION

Additional supporting information may be found in the online version of this article.

Table S1 Samples used in this study.

Fig. S1. Isheyevu powder XRD.

Fig. S2. Troilite powder XRD.

Fig. S3. Other sulfide powder XRD.

Fig. S4. Mayo Belwa (aubrite).

Fig. S5. Aubres (aubrite).

Fig. S6. Khor Temiki (aubrite).

Fig. S7. Norton County (aubrite).

Fig. S8. Shallowater (aubrite).

Fig. S9. NWA 5492 (ungrouped chondrite).

Fig. S10. Hammadah al Hamra 237 (CBb chondrite).

Fig. S11. Quebrada Chimborazo 001 (CBa chondrite).

Fig. S12. Isheyevu (CH/CBb chondrite).

Fig. S13. NWA 12273 (ungrouped chondrite).

Fig. S14. Sample near-IR slope (760–1200 nm) versus band center.

Fig. S15. Phase angle versus spectral slope for Isheyevu powder.

Fig. S16. Phase angle versus spectral slope for Nantan FeS powder.

Fig. S17. Phase angle versus spectral slope for Minas Gerais pyrrhotite powder.

Fig. S18. Phase angle versus spectral slope for Norilsk pentlandite/chalcocopyrite powder.